Article

DFT Study of Heteronuclear (TMFeO$_3$)$_x$ Molecular Clusters (Where TM = Sc, Ti, Fe and x = 2, 4, 8) for Photocatalytic and Photovoltaic Applications

Abdul Majid [1,*], Sidra Arif [1], Tariq M. Younes [2], Mohammad Alkhedher [3] and Sayed M. ElDin [4]

1   Department of Physics, University of Gujrat, Gujrat 50700, Pakistan
2   Department of Mechatronics Engineering, Faculty of Engineering Technology, Al Balqa Applied University, Amman 19117, Jordan
3   Mechanical and Industrial Engineering Department, Abu Dhabi University, Abu Dhabi 111188, United Arab Emirates
4   Center of Research, Faculty of Engineering & Technology, Future University in Egypt, New Cairo 11835, Egypt
*   Correspondence: abdulmajid40@uog.edu.pk

Abstract: The computational modeling of metal oxide clusters for photovoltaic application is carried out by using density functional theory. The structural and electronic properties of heteronuclear (TMFeO$_3$)$_x$ molecular clusters (where x = 2, 4, 8 and TM = Sc, Ti, Fe) are investigated in detail. The physical parameters such as energy gap, formation energy, binding energy, and stability are determined. The computed values and trends in electronegativity (χ), chemical potential (μ), hardness (η) and softness (S), positions of highest occupied molecular orbitals (HOMO) and lowest unoccupied molecular orbitals (LUMO), and HOMO-LUMO gap with varying cluster sizes are discussed. The iso-surface plots with relaxed structure related to the frontier MOs are described to shed light on the charge transfer mechanism. In the entire series of the studied clusters, the computed gap of (Fe$_2$O$_3$)$_8$ was found minimal and thus suitable for red light absorption, whereas (TiFeO$_3$)$_2$ exhibited a maximum gap which shows potential for blue light absorption. The clusters exhibiting different values of the gap are found suitable to absorb the solar radiation. HOMO and LUMO position with their energy differences in the clusters are found compatible for applications in photocatalytic and photovoltaic applications. The observed trend in the computed parameters points to the potential of the simulated materials for application in a TiO$_2$-based semiconducting photoanode to harvest sunlight.

Keywords: clusters; HOMO; LUMO; DFT; photoanode

1. Introduction

Researchers and innovators are extensively working to realize new functional materials for applications in diverse fields [1–3]. The clusters being molecule-to-bulk intermediary structures opened up multidisciplinary research areas which have been of prime interest to theoretical as well as experimental researchers. The investigations of the clusters have been found fruitful not only to understand basic physics and chemistry of the materials for shedding light on unclear mysteries but also to explore new applications. Owing to recent improvement in synthesis techniques, the investigation of different types of clusters and nanomaterials have been observed [4–6]. Moreover, with the availability of ever-efficient resourceful computing hardware, along with public access to powerful codes, the study of accurate properties of different clusters with size-dependent properties has become possible. The computational simulation of molecular clusters using first principles methods caught wide research attention in recent years [7]. The strategies have been found worthwhile due to precise prediction of the variety of the clusters exhibiting potential for electronic, optoelectronic, spintronic, photovoltaic, biomedical, and energy devices [8–12].

Metal oxide clusters (MOCs) are potential candidates for surface-sensitive applications due to their exceptional structures, transport, active sites, chemisorption, and charge

transfer properties. The MOCs such as Zr_6O_8, M(OH) with metals such as Al, Cr, Fe, and Zn_4O, M_3O with metals such as Al, Fe, Cr, and $Ti_4O_8(OH)_4$, and Mn_4CaO_5 have been found useful for catalytic applications [13]. The anionic inorganic MOCs in nanometer size appeared to offer a framework for high-density data storage utilized in memory elements [14]. The noble-metal-doped heteronuclear MOCs have shown potential for heterogeneous catalysis when investigated for catalytic CO oxidation [15]. It has been shown that carbon-doped alkaline-earth MOCs exhibit donor and acceptor characters which appeared to enhance photocatalytic activities of the materials [16]. In addition to MOCs, transition metal oxide (TMO) clusters have been found to be valuable materials to further understand the surface-sensitive scientific mechanism. For example, the role of surface and structure in reactive catalytic materials is not well understood. There has been great research interest to utilize TMOs with variable cations, size, composition, charge, and oxidation states to explore new applications on the basis of their structure–property relationship [17,18].

The heteronuclear and mononuclear TMOCs involving 3d and 4d elements have caught significant research interest due to magnetic, optical, optoelectronic, and electrochemical properties. Out of diverse types of TMOCs, hematite (Fe_2O_3) clusters exhibited exceptional potential for applications in photocatalysis [19], photovoltaics [20], water oxidation [21], thermal recycling [22], electrodes in lithium-ion batteries [23], magnetics [24], etc. It has been shown that Fe_2O_3 can be used as counter electrode in dye-sensitized solar cells for charge transfer [25].

Hematite is a potential candidate for use as photocatalyst to split water; however, its performance as a photoanode needs further improvement [26]. In order to modify properties of hematite, several strategies including surface modification, doping, composite formation, alloying, and heterojunctions have been utilized [27]. Like those of other metal oxides, the properties of Fe_2O_3 change upon doping. It has been reported that Mn doping at 3–5% doping concentration improves catalytic activity of γ-Fe_2O_3 [28]. TiO_2-doped hematite has shown potential for application in solar energy conversion with good charge transfer characteristics [29]. The efforts on tuning the characteristics of different materials upon doping for improvement in optoelectronic properties have been reported [30].

The majority of potential photovoltaic materials often experience quick recombination rates of electron–hole pairs which degrade the functioning of the device [31,32]. To overcome the degradation mechanism, the suitable choice of materials, doping conditions, and synthesis strategies need to be optimized in order to prevent the motion of electrons towards the hole to reduce chances of recombination. It has been demonstrated that doping of ZnO causes reduction in the photogenerated electron–hole recombination rate [33]. The suppression of e-h recombination rate in TiO_2 nanowires upon treatment with hydrogen to produce oxygen-deficient arrays has been reported [34]. The doping of copper ferrite nanocrystals with Al via the solid-state route has exhibited a reduction in e-h recombination for use in photocatalytic applications [35]. In order to improve the photocatalytic performance, the suppression of the e-h recombination rate in graphitic carbon nitride modified via polymers has been achieved [36]. For the same purpose, the present work is computationally carried out by designing different sized $(TMFeO_3)_x$, where TM = Sc, Ti, Fe and x = 2, 4, 8. The calculations are performed on the series of TMOCs using a density functional tight bonding (DFTB) model with $GFN_{1-x}TB$ as the correlation function. The computed structural, energetic, electronic, and photoelectric properties of the simulated clusters revealed favorable results to utilize the materials in the photoanode.

2. Computational Details

The entire calculations reported herein were performed using the DFTB approach of density functional theory (DFT) through AMS (Amsterdam Modeling Suit) of SCM (software for chemistry and materials) code [37]. The DFTB computations were carried out using $GFN_{1-X}TB$ (Grimme's first function extended tight binding) which has been found to offer accurate predictions [38].

The calculations were spin unrestricted with Slater–Koster approximation including D4 dispersion. The tasks include geometry optimization, PES scans, single point calculations, and transition state search. Further, we studied properties such as dipole moment, atomic charge analysis, Hessian field analysis, and magnetic moments. The Grimme's first generation extended tight binding ($GFN_{1-x}TB$) Hamiltonian approach was used for fast preliminary calculations. It used Slater orbitals for the calculation of the Hamiltonian and optimization of geometries of the structures. DFTB with auto-selected D_3-B_J dispersion correction was utilized for the clusters. In order to simulate different numbers of unpaired electrons, the SSC strategy was selected as 'Auto'. Otherwise, its value for relative distribution of electrons was set either to 'Fermi' or 'Aufbau'.

Geometry optimization of the clusters was carried out to determine relaxed structure that determines minimum energy configurations. The single point (SP) calculation on the optimized geometries was carried out to determine electronic and magnetic properties of the clusters. The binding energies/formation energy for the clusters were computed using Equation (1):

$$E_F = E(TMFeO_3) - xE_{TM} - xE_{Fe} - 3xE_o \tag{1}$$

where TM = Sc, Ti, Fe and x = 2, 4, 8 for these coordinated compounds prepared via reaction $TM + FeO + O_2 \rightarrow TM(Fe)O_3$.

The values of chemical potential, electronegativity, chemical stability, hardness, and softness of the materials were also determined. In these expressions, ionization potential (IP) is the amount of energy required to free an electron from a gaseous molecule, i.e., E_{HOMO}, whereas electron affinity (EA) is the amount of energy that is used to add an electron to a gaseous molecule, i.e., E_{LUMO}. The formulas used to calculate chemical potential, electronegativity, hardness, and softness are given by the respective relations $\mu = -\frac{IP+EA}{2}$ (eV), $\chi = \frac{IP+EA}{2}$ (eV), $\eta = \frac{IP-EA}{2}$ (eV), and $S = \frac{1}{2\eta}$ (eV).

The calculations were carried out using Slater-type basis sets at the TZ2P (Triple-Zeta with double polarization) level. The value of energy convergence criteria during was set to 10^{-6} eV/molecule. Considering the involvement of open shell atoms, the calculations were carried out by employing unrestricted mode to include spin polarization by assuming possible values of magnetic moment on the clusters. To study optical or optoelectronic properties of the mentioned clusters, UV/VIS Spectroscopy was performed to compute oscillator strength as a function of incident solar rations using the DFTB approach. The excited states of the clusters were computed for the allowed transition in case of singlet and triplet states by employing the Davidson algorithm.

3. Results and Discussion

The computed results and discussions are described in the following sections.

3.1. Structural Properties of $(TMFeO_3)_x$ Molecular Clusters

The optimized structures of the clusters with minimum energy for $(TMFeO_3)_x$ where TM = Sc, Ti, Fe and x = 2, 4, 8 are shown in Figure 1. The calculated values of bond energy per $ScFeO_3$ found using Equation (1) are −98.720 eV, −99.035 eV, and −99.22 eV for $(ScFeO_3)_2$, $(ScFeO_3)_4$, and $(ScFeO_3)_8$, respectively.

In the case of $(TiFeO_3)_2$, values of bond energy per $TiFeO_3$ are found as −93.04 eV, −100.13 eV, and −100.36 eV for $(TiFeO_3)_2$, $(TiFeO_3)_4$, and $(TiFeO_3)_8$, respectively. Finally, the values of bond energy per Fe_2O_3 are found as −1087.5 eV, −1088.55 eV, and −1089.27 eV for $(Fe_2O_3)_2$, $(Fe_2O_3)_4$, and $(Fe_2O_3)_8$, respectively. In the case of Fe_2O_3 clusters, the energy difference is very small in starting structures but afterwards it increases with further increase in size of the clusters. The trend indicates that energy is consistently decreasing and hence the clusters with bigger sizes are energetically more favorable. It points to the feasibility of multiplication of these clusters to grow practical-sized structures for practical applications [39]. The values of bond energy computed for the series of clusters are given in Figure 2. The calculated values of bond energy, binding energy, and formation energy for the series of clusters are given in Table 1.
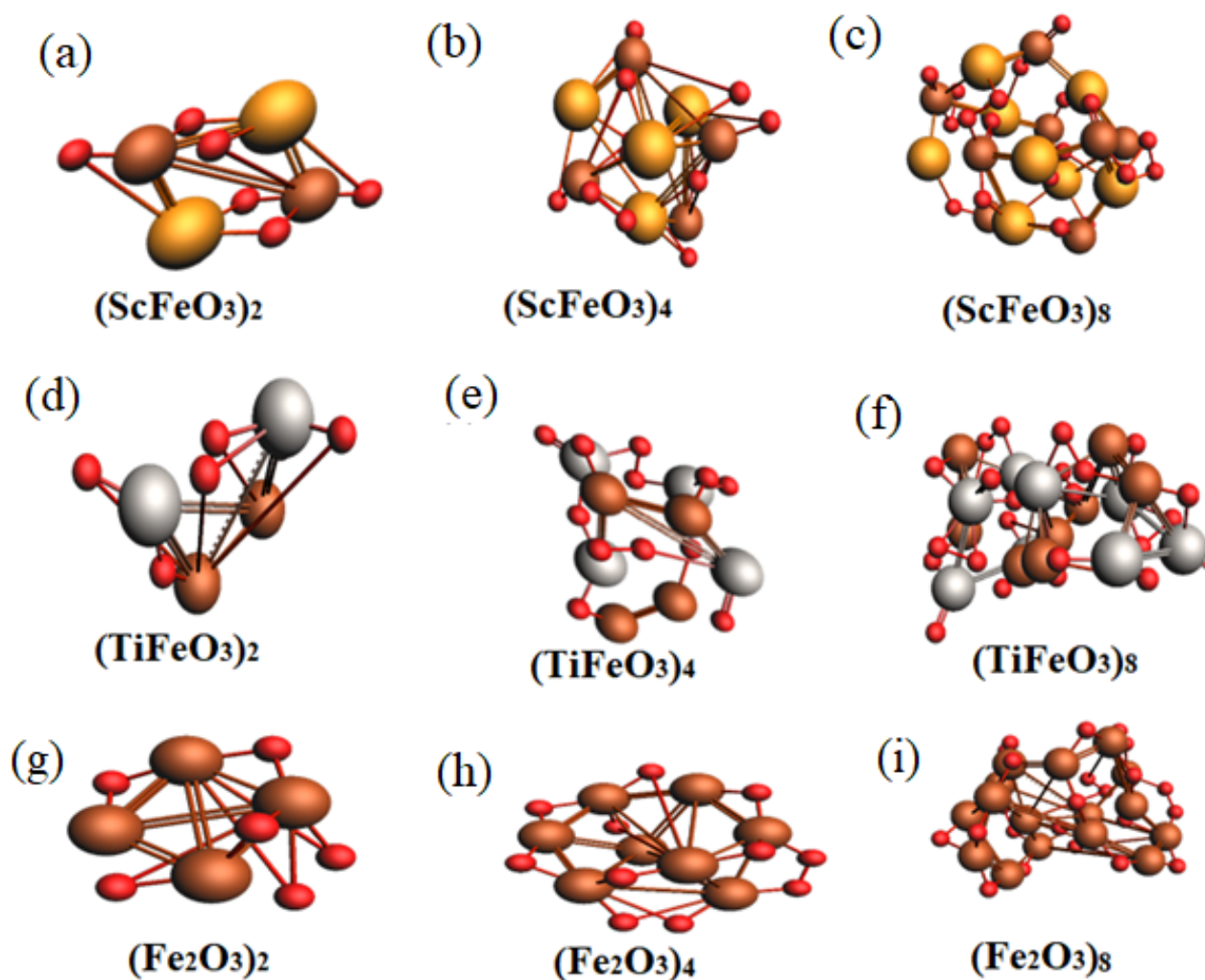
Figure 1. Optimized structures of $(TMFeO_3)_x$ molecular clusters for x = 2, 4, 8 and TM = Sc, Ti, Fe showing geometry of the clusters (**a**) $(ScFeO_3)_2$, (**b**) $(ScFeO_3)_4$, (**c**) $(ScFeO_3)_8$, (**d**) $(TiFeO_3)_2$, (**e**) $(TiFeO_3)_4$, (**f**) $(TiFeO_3)_8$, (**g**) $(Fe_2O_3)_2$, (**h**) $(Fe_2O_3)_4$, and (**i**) $(Fe_2O_3)_8$.

Table 1. This Table Explains Tabular form of Spin, Total Optimized Energy, Fermi Energy at Optimized Energy, Binding Energy, and Formation Energy for all Calculated Clusters.

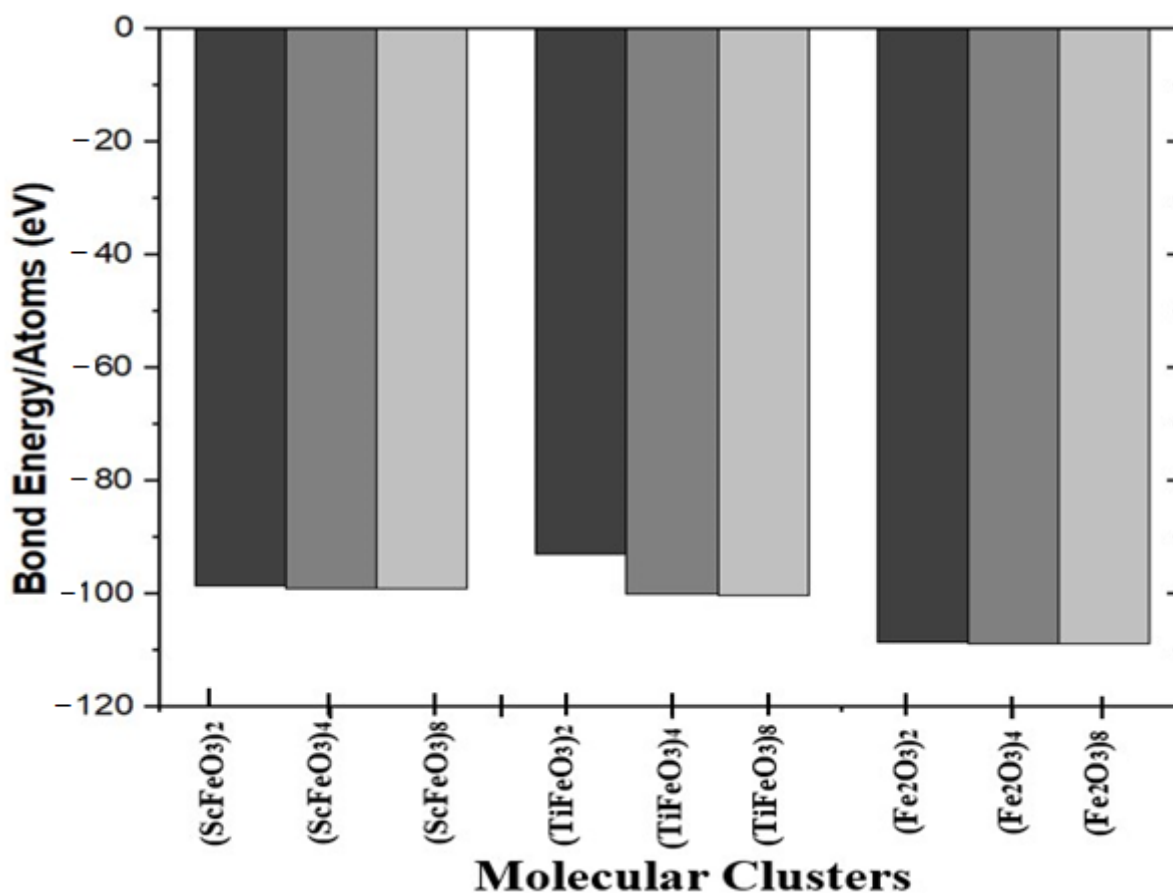| Molecular Clusters	Bond Energy (eV)	Binding Energy (eV)	Formation Energy E_F (eV)
$(ScFeO_3)_2$	−987.20	25.114	−25.114
$(ScFeO_3)_4$	−1980.7	56.538	−56.538
$(ScFeO_3)_8$	−3968.8	120.49	−120.49
$(TiFeO_3)_2$	−930.047	24.394	−24.394
$(TiFeO_3)_4$	−2002.7	65.438	−65.438
$(TiFeO_3)_8$	−4014.7	140.14	−140.14
$(Fe_2O_3)_2$	−1087.5	33.638	−33.638
$(Fe_2O_3)_4$	−2177.1	62.256	−62.256
$(Fe_2O_3)_8$	−4357.1	141.47	−141.47

Figure 2. The computed values of bond energy for all molecular clusters of $(TMFeO_3)_x$, where TM = Sc, Ti, Fe and x = 2, 4, 8.

The formation for these clusters takes place after relevant phase transition to configure a new set of relaxed structures [40]. The values of formation energy determined using Equation (1) are found as -25.114 eV, -56.538 eV, and -120.49 eV for the respective clusters of $(ScFeO_3)_X$ for x = 2, 4, 8. The bridge-like structure of the starting clusters is changed to complex formation. The values for formation energy for $(TiFeO_3)_x$ for x = 2, 4, 8 are found as -24.394 eV, -65.438 eV, and -140.14 eV, respectively. The values of formation energy calculated for $(Fe_2O_3)_x$ for x = 2, 4, 8 are -33.63 eV, -69.25 eV, and -141.47 eV, respectively. The binding energy sheds light on the dissembling of system of particles into their constituents such as TM, Fe, and O [41]. The values of binding energy calculated for the clusters are shown in Table 1, according to which $(ScFeO_3)_x$ for x = 2, 4, 8 exhibits the respective values of 25.11eV, 56.53 eV, and 120.49 eV. For $(TMFeO_3)_x$ with TM = Ti, Fe and x = 2, 4, and 8, the respective values of E_B are 24.39 eV, 65.43 eV, and 140.14 eV and 33.63 eV, 69.25 eV, and 141.47 eV.

It is observed that electrons are transferred from TM atoms to Fe and oxygen as per the literature [42]. The dipole moment computed for $(Fe_2O_3)_2$ clusters is 0.936 D, which is enhanced to 3.39 D and 6.63 D for the clusters $(Fe_2O_3)_4$ and $(Fe_2O_3)_8$, respectively. Similarly, in the case of $(TMFeO_3)_x$, where TM = Sc, due to the difference in number of unpaired electron (charge) electrons, Ti moves from TM to Fe and hence to oxygen atoms. For $(ScFeO_3)_2$, the dipole moment is 0.052 D, which is enhanced to 7.09 D and 7.18 D for the clusters $(ScFeO_3)_4$ and $(ScFeO_3)_8$, respectively. Finally, in the case of $(TiFeO_3)_2$, the dipole moment is 2.21 D, which is enhanced to 6.637 D and 9.11 D for the clusters $(TiFeO_3)_4$ and $(TiFeO_3)_8$, respectively. The trend in dipole moment of the clusters is sketched in Figure 3.
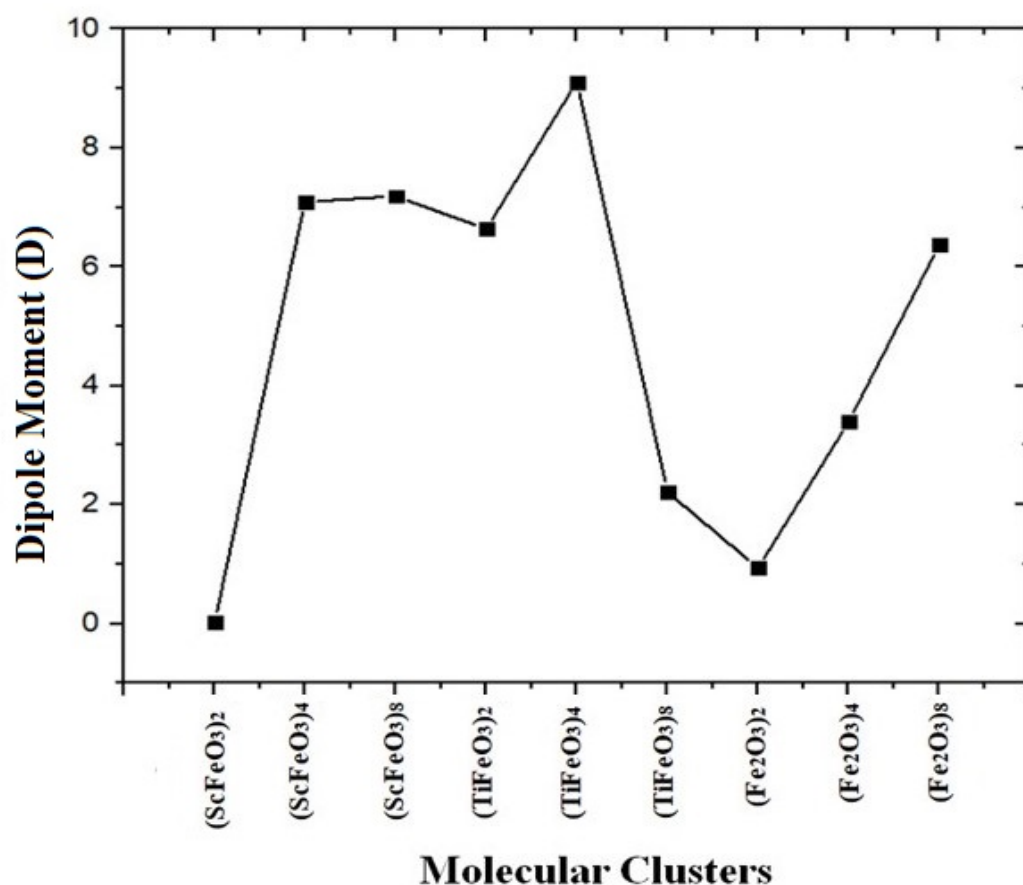
Figure 3. The calculated values of dipole moment (D) for [(TMFeO$_3$)]$_x$ molecular clusters for x = 2, 4, 8 and TM = Sc, Ti, Fe.

3.2. Electronic Properties of $(TMFeO_3)_x$ *Molecular Clusters*

The electrical properties are owed to chemical stability and reactivity of materials which depend upon electronegativity (χ), chemical potential (μ), and softness (S) and hardness (H) of materials. These electronic parameters are computed using frontier molecular orbitals, i.e., highest occupied molecular orbital (HOMO), lowest unoccupied molecular orbital (LUMO), and iso-surface plots. The interactions of electrons and occupancies are shown on iso-surface plots by labeling energy levels. The parameters were calculated using HOMO and LUMO energy level values on iso-surface plots. HOMO energy corresponds to ionization potential (IP) and LUMO energy value refers to electron affinity (EA) of the clusters. The computed electronic parameters with HOMO-LUMO energies and their band gap for all studied molecular clusters are given in Table 2.

The electronegativity of the (ScFeO$_3$)$_2$ cluster comprising Sc, Fe, and three oxygen atoms is found to be -12.68 eV, which agrees with the literature [43]. The value of the HOMO-LUMO gap for all clusters is different but a trend is observed in such a way that the value is observed to decrease with the size of the clusters, with the exception of cluster (ScFeO$_3$)$_x$. HOMO and HOMO-1 values for (ScFeO$_3$)$_2$ are -13.72 eV and -13.74 eV, while for LUMO and LUMO+1 are -11.64 eV and -11.62 eV, respectively. The contribution of Sc atoms due to higher charge densities is at the maximum level (59.4%) compared to Fe atoms (13.67%) and O atoms (13.97%). The electronic charge is transferred from Sc to Fe and from Fe to oxygen atoms. The contribution of electronic charge transfer is observed to increase with respect to the cluster size; that is, for Sc4 there is a 63.4% enhancement, while for Sc8 there is a 65.6% enhancement. The contributions from Sc, Fe$_4$, and Fe$_8$ dominate, whereas O$_{12}$ and O$_{24}$ correspond to contributions 25.35% and 28.5% for (ScFeO$_3$)$_4$ and (ScFeO$_3$)$_8$, respectively.

Table 2. Calculated values of HOMO, LUMO, HOMO-LUMO gap, electronegativity (χ), hardness (η), chemical potential (μ), and softness (S) for molecular clusters $(TMFeO_3)_x$.

Molecular Clusters	EA (eV)	IP (eV)	B.G. (eV)	η (eV)	S (eV)	μ (eV)	X (eV)
$(ScFeO_3)_2$	−11.64	−13.72	2.08	−1.04	−0.48	12.68	−12.68
$(ScFeO_3)_4$	−10.68	−13.21	2.53	−1.26	−0.39	11.94	−11.94
$(ScFeO_3)_8$	−10.95	−12.99	2.04	−0.02	−22.0	11.97	−11.97
$(TiFeO_3)_2$	−11.09	−13.68	2.59	−1.29	−0.38	12.38	−12.38
$(TiFeO_3)_4$	−12.01	−14.05	2.04	−1.02	−0.49	13.03	−13.03
$(TiFeO_3)_8$	−11.33	−13.38	2.05	−1.02	−0.49	12.35	−12.35
$(Fe_2O_3)_2$	−13.41	−15.58	2.17	−1.05	−0.47	14.49	−14.49
$(Fe_2O_3)_4$	−13.55	−15.64	2.08	−1.04	−0.48	14.59	−14.59
$(Fe_2O_3)_8$	−13.34	−15.27	1.92	−0.96	−0.52	14.30	−14.30

In the case of $(ScFeO_3)_4$ and $(ScFeO_3)_8$, HOMO and HOMO-1 energy values are −13.21 eV and −13.23 eV and −12.99 eV and −13.01 eV, respectively. LUMO and LUMO+1 for both these clusters are at −10.68 eV and −10.65 eV and −10.95 eV and −10.91 eV, respectively. The computed values of electronegativity and chemical potential for the series of studied clusters is shown in Figure 4.
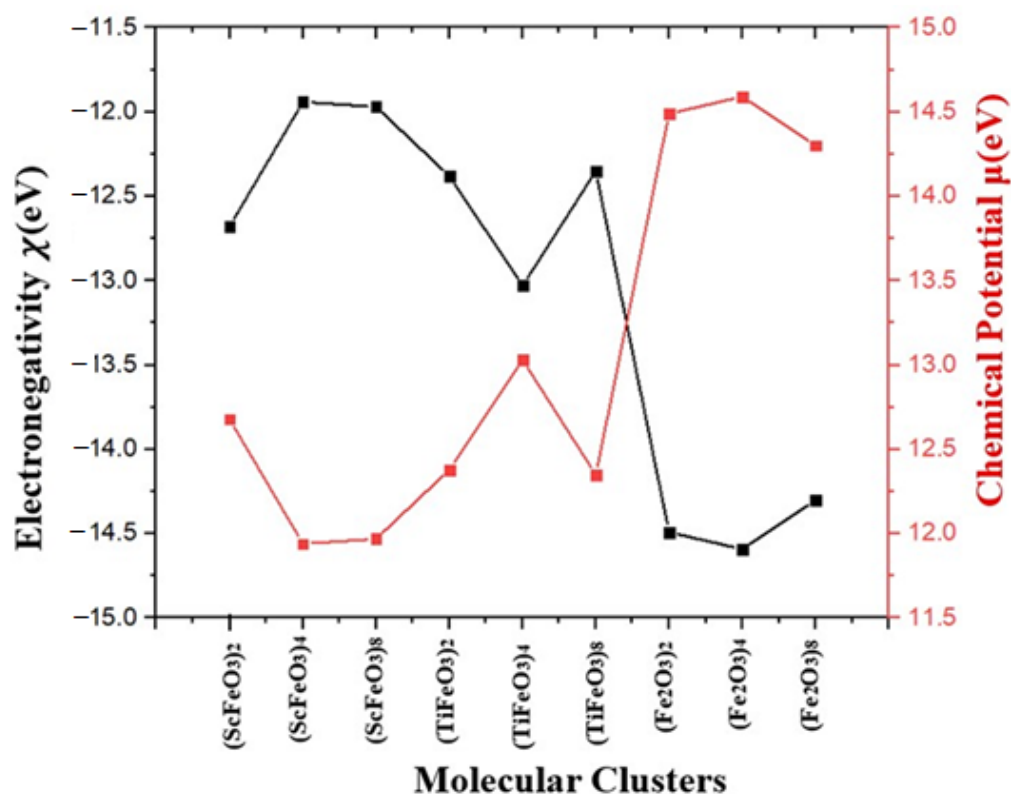
Figure 4. The computed values of electronegativity and chemical potential for $(TMFeO_3)_x$ molecular clusters where x = 2, 4, 8 and TM = Sc, Ti, and Fe.

Similarly, corresponding values of the HOMO and HOMO-1 energy levels for $(TiFeO_3)_{2,4,8}$ molecular clusters are −13.68 eV and −14.05 eV, −13.38 eV and 13.71 eV, and −14.09 eV and −13.36 eV, respectively. LUMO and LUMO+1 values for $(TiFeO_3)_{2,4,8}$ clusters are −11.09 eV, −12.01 eV, and −11.33 eV and −11.05 eV, −11.98 eV, and −11.30 eV, respectively.

Since Ti is more electropositive than Fe and Fe is more electropositive than O, an electron moves from Ti to Fe and hence from Fe to O. The contribution of the electron transfer rate for Ti is about 49.38%, 52.12%, and 51.67% and for Fe is 28.21%, 24.46%, and

27.99% for the respective clusters $(TiFeO_3)_{2,4,8}$. The number of unpaired electrons in Ti lies between Sc and Fe, due to which it is more electropositive than Fe and thus electrons transfer from Ti to Fe and then to O. The computed values showing trend of softness (eV) and hardness (eV) for the entire series of the clusters are given in Figure 5.
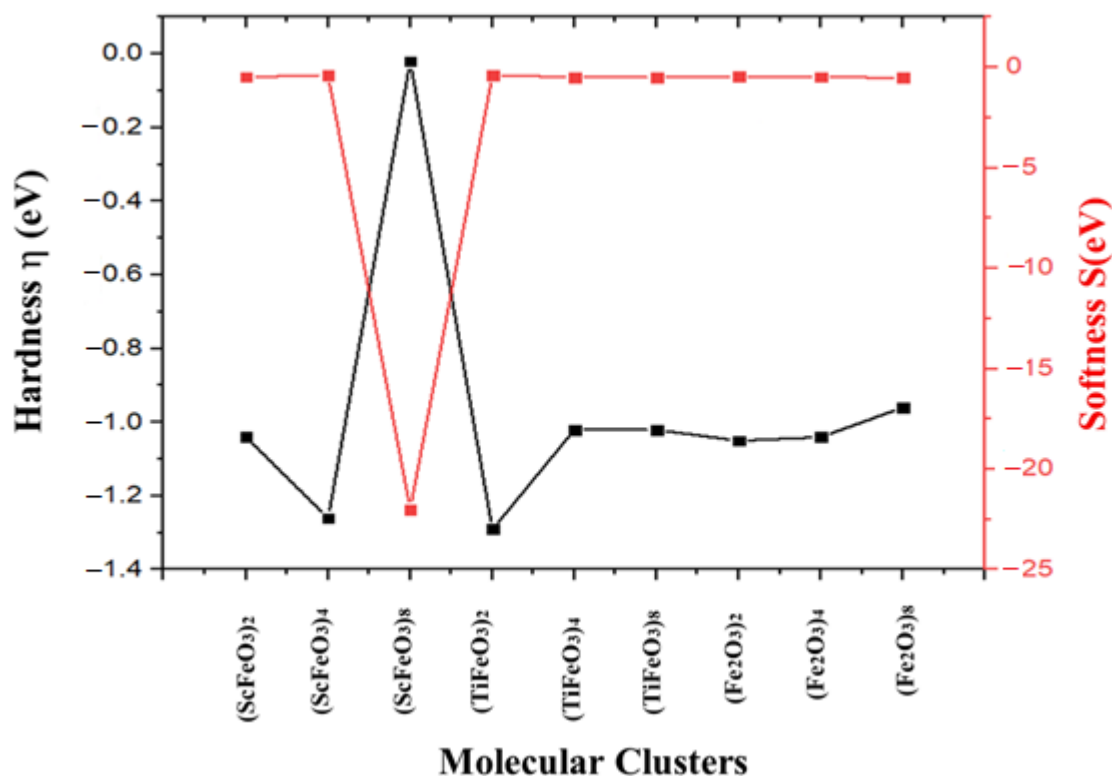

Figure 5. The computed values of softness and hardness for $(TMFeO_3)_x$ molecular clusters where x = 2, 4, 8 and TM = Sc, Ti, and Fe.

It is observed that $(ScFeO_3)_8$ is harder and least stable, due to which it is more reactive toward electrophilic catalysis in comparison to all studied clusters. However, the material's softness decreases (hardness increases) with the increase in cation atomic size in the clusters. The softness is related to bond order at the atomic level and causes material deformation on the application of force [44]. The values of the two highest occupied energy levels of HOMO and HOMO-1 and two lowest unoccupied energy levels for all nine clusters of the transition metals complex are shown in Figure 6.

The transition-metal-based oxide clusters may have complex stable structure applications oriented to various properties due to hybrid d and s orbitals [45]. Owing to the computed properties, the mentioned molecular clusters are potential candidates for applications in photovoltaics and photocatalytic applications [46]. The adsorption of transition metal clusters on a semiconducting material such as TiO_2 causes a narrowing of band gap energy which brings UV absorption into the visible region of the electromagnetic spectrum.

The results indicated that the HOMO of $(ScFeO_3)_2$ obtained maximum contribution from cationic 3d orbitals. It is observed that $Sc\text{-}3d_{xy}$ carries a 69.4% contribution due to one unpaired electron in the outer shell, whereas Fe subshells 3d and 4s offer contributions of only 13.4%. Likewise, $2P_x$, $2P_y$, and $2P_z$ orbitals of all oxygen atoms in the clusters carry an 18.2% contribution. In the case of $(ScFeO_3)_2$, LUMO and LUMO+1 obtained major contribution (i.e., 56.7%) from $Fe\text{-}3d_{yz}$ and $3d_{x^2\text{-}y^2}$ subshells, with the role of $Sc\text{-}3d_{xy}$ at 14.5% and $O_6\text{-}2p$ sublevels contributing 26.7%.
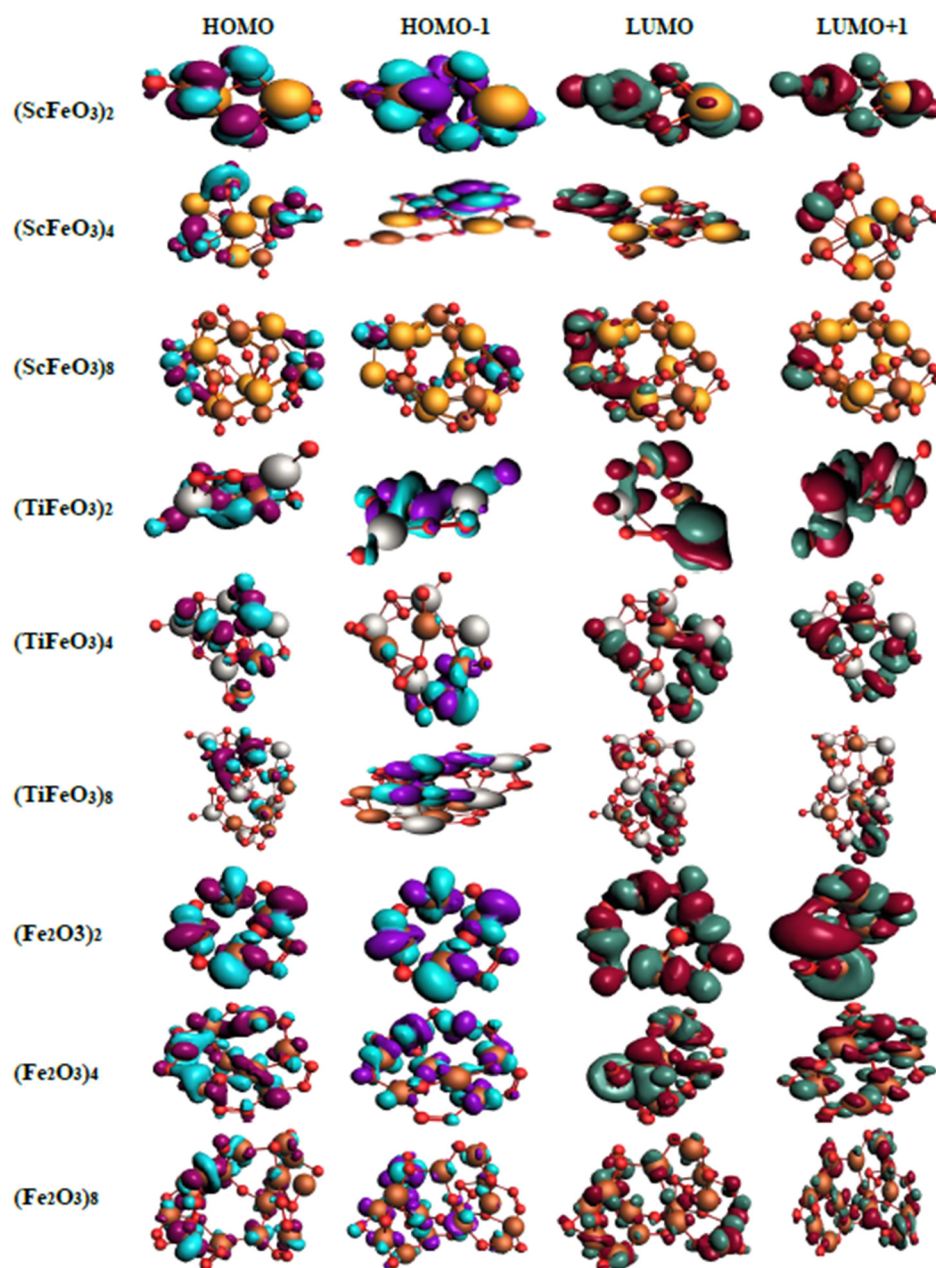
Figure 6. Iso-surface plots for highest occupied energy levels HOMO and HOMO-1 and lowest unoccupied energy levels LUMO and LUMO+1.

Similarly, for $(ScFeO_3)_4$ and $(ScFeO_3)_8$, the corresponding HOMO and HOMO-1 states obtained major contributions of 63.3%, 69.3%, and 51.4%, 48.5% from Sc-$3d_{xy}$ orbitals, respectively, whereas 35.4% and 27.4% and 29.58% and 39.5% contributions were observed from Fe-$3d_{xy}$ and $3z^2$ atomic states in HOMO and HOMO-1 states of these clusters. Likewise, for $(TMFeO_3)_x$ x = 2, 4, 8 molecular clusters, the corresponding energy levels HOMO and HOMO-1 are located at −13.68 eV, −14.05 eV, and −13.38 eV and −13.71 eV, −14.06 eV, and −13.40 eV, respectively. Ti ($3d^2 4s^2$) has two unpaired electrons in states $3d_{xy}$ and $3d_{yz}$. The Ti contribution for HOMO and HOMO-1 is 63.4%, 53.4%, and 51.4% and 49.5%, 37.5%, and 39.53% for $(TiFeO_3)_x$ x = 2, 4, 8 clusters, respectively. The electrons move firstly from Ti atoms to Fe atoms and then to oxygen atoms. The contributions from Fe atoms are about 33.3%, 39.4%, and 29.99% for HOMO and 29.4%, 29.1%, and 26.19% for HOMO-1 states, respectively.

For $(Fe_2O_3)_{2,4,8}$ clusters, HOMO and HOMO-1 levels are found at -15.58 eV, -15.64 eV, and -15.27 eV and -15.56 eV, -15.67 eV, and -15.28 eV, respectively. In the HOMO of $(Fe_2O_3)_{2,4,8}$, the main contributions of 67.39%, 62.5%, and 67.45% are due to Fe-3d states and 31.39%, 37.4%, and 29.1% due to oxygen P_x, P_y, and P_z. The LUMO and LUMO+1 levels mainly related to oxygen atoms in the clusters play a main role in accepting electrons. The O-2P orbitals having unoccupied states are most likely to receive incoming electrons, and likewise the role of Fe d_{yz}, $d_x{}^2$-$_y{}^2$ and $d_z{}^2$ states is also important. The contributions of P orbitals in the LUMO of $(Fe_2O_3)_{2,4,8}$ are 49.9%, 52.6%, and 47.46% and for LUMO+1 the values are 47.2%, 49.9%, and 42.34% respectively.

The contribution from cation 3d orbitals is observed increased when the size of the clusters is increased in all cases. The computed results indicated that $(TiFeO_3)_2$ is least reactive and $(Fe_2O_3)_8$ is more suitable for operation with a TiO_2-based photoanode. The comparative view of HOMO and LUMO energy levels with their band gaps positioned relative to normal hydrogen electrode potential is shown in Figure 7. The photocatalytic water splitting requires semiconductors having band gaps greater than 1.23 eV with CBM and VBM straddling the respective hydrogen evolution reaction and oxygen evolution reaction [47,48]. Thus, the investigated clusters seem to offer tunable electronic structure for use in photocatalytic applications.
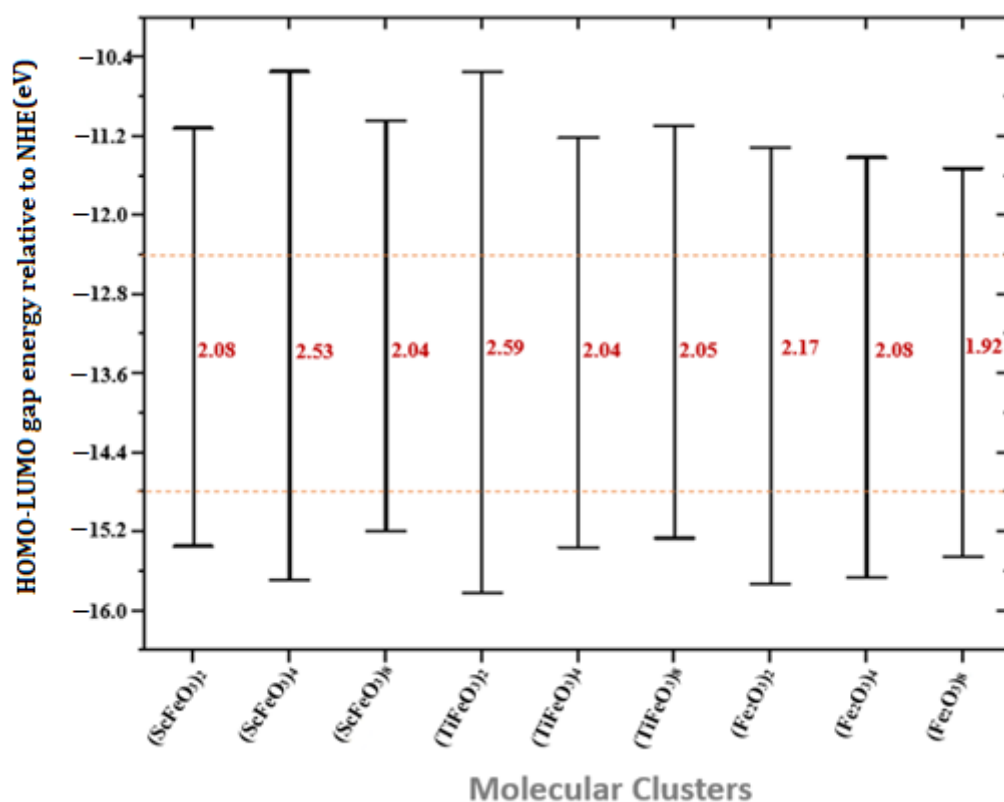

Figure 7. The computed values of gap with HOMO and LUMO positioned relative to normal hydrogen electrode for $(TMFeO_3)_x$ clusters with x = 2, 4, 8 and TM = Sc, Ti, Fe.

Out of all these nine clusters, it is seen from Figure 7 that $(Fe_2O_3)_8$ is more suitable for red light absorption. The increase in size of the clusters appeared to increase the gap, which points to a tunable gap for visible light absorption. On the other extreme, the cluster $(TiFeO_3)_2$ has a maximum gap energy of 2.59 eV, which may absorb blue light for application as a photoanode. Thus, different studied clusters fall in different regions of the electromagnetic spectrum to absorb solar radiation. However, if problems with the gap compatibility exist, the issue may be resolved by adsorption of these molecular clusters on the TiO_2 slab to prepare the photoanode [49]. As a result, an efficient photoanode may be

prepared with decreased electron–hole recombination and an increase in electron injection rate towards the outer circuit [50,51]. The study of these clusters adsorbed on TiO_2 slabs for the applications will be reported elsewhere.

4. Conclusions

The electronic, structural, and optical properties of all molecular clusters were computed by using the DFTB model. The work reported in this paper points out that $(TMFeO_3)_x$ molecular clusters with varying values of x and TM yield an efficient semiconducting material mechanism. The extracted results on formation energy, adsorption energy, binding energy, and magnetic spin moment describes these properties. The photoanode based on these clusters is efficient for photovoltaic devices, especially for solar cells that absorb light for ultraviolet to visible light. A key finding in this study is the inverse relationship of molecular cluster size to the total optimized energies (dispersion energy, Columbic energy, etc.). $(TiFeO_3)_8$ was found to be the most stable and best potential semiconducting material of all clusters studied, owing to maximum formation energy, dipole moment, and the gap energies.

Author Contributions: Data curation, S.A.; Formal analysis, A.M. and S.A.; Investigation, T.M.Y. and M.A.; Methodology, A.M. and S.M.E.; Supervision, A.M.; Validation, T.M.Y. and M.A.; Visualization, S.M.E.; Writing—original draft, A.M. and S.A.; Writing—review & editing, T.M.Y., M.A. and S.M.E. All authors have read and agreed to the published version of the manuscript.

Conflicts of Interest: The authors declare no conflict of interest.

References

1. Liu, W.-J.; Jiang, H.; Yu, H.-Q. Development of Biochar-Based Functional Materials: Toward a Sustainable Platform Carbon Material. *Chem. Rev.* **2015**, *115*, 12251–12285. [CrossRef]
2. Ibrahim, M.E.; Eldin, E.T.; Elzoghby, S.F.; Izzularab, M.A.; Abd-Elhady, A.M. The Role of the Accumulated Surface Charge on Nanoparticles in Improving the Breakdown Strength of Liquid and Solid Insulation. *Energies* **2022**, *15*, 4860. [CrossRef]
3. Guedri, K.; Raizah, Z.; Tag-Eldin, E.; Ashraf, W.; Khan, U.; Galal, A.M. Thermal efficiency in hybrid (Al_2O_3-CuO/H_2O) and tri-hybrid (Al_2O_3-CuO-Cu/H_2O) nanofluids between converging/diverging channel with viscous dissipation function: Numerical analysis. *Front. Chem.* **2022**, *10*, 960369.
4. Lu, Y.; Chen, W. Sub-nanometre sized metal clusters: From synthetic challenges to the unique property discoveries. *Chem. Soc. Rev.* **2012**, *41*, 3594–3623. [CrossRef] [PubMed]
5. Fan, Y.; Liu, S.; Yi, Y.; Rong, H.; Zhang, J. Catalytic nanomaterials toward atomic levels for biomedical applications: From metal clusters to single-atom catalysts. *ACS Nano* **2021**, *15*, 2005–2037. [CrossRef]
6. Abbas, Q.; Siyal, S.H.; Mateen, A.; Hassan, N.U.; Idrees, A.; Rehman, Z.U.; El Din, E.M.T.; Bajaber, M.A.; Javed, M.S. Hydrothermal Synthesis of Binder-Free Metallic $NiCo_2O_4$ Nano-Needles Supported on Carbon Cloth as an Advanced Electrode for Supercapacitor Applications. *Materials* **2022**, *15*, 4499. [CrossRef]
7. Zhao, X.; Pei, G.; Xu, S.; Kong, C.; Yang, Z.; Yang, T. Endohedral group-14-element clusters TM@E9 (TM = Co, Ni, Cu; E = Ge, Sn, Pb) and their low-dimensional nanostructures: A first-principles study. *Phys. Chem. Chem. Phys.* **2021**, *23*, 20654–20665. [CrossRef]
8. Kawasaki, N.; Wang, H.; Nakanishi, R.; Hamanaka, S.; Kitaura, R.; Shinohara, H.; Yokoyama, T.; Yoshikawa, H.; Awaga, K. Nanohybridization of Polyoxometalate Clusters and Single-Wall Carbon Nanotubes: Applications in Molecular Cluster Batteries. *Angew. Chem.* **2011**, *123*, 3533–3536. [CrossRef]
9. Hang, X.; Bi, Y. Thiacalix [4] arene-supported molecular clusters for catalytic applications. *Dalton Trans.* **2021**, *50*, 3749–3758. [CrossRef]
10. Sgibnev, Y.; Cattaruzza, E.; Dubrovin, V.; Vasilev, V.; Nikonorov, N. Photo-Thermo-Refractive Glasses Doped with Silver Molecular Clusters as Luminescence Downshifting Material for Photovoltaic Applications. *Part. Part. Syst. Charact.* **2018**, *35*. [CrossRef]
11. Alberi, K.; Nardelli, M.B.; Zakutayev, A.; Mitas, L.; Curtarolo, S.; Jain, A.; Perkins, J. The 2019 materials by design roadmap. *J. Phys. D Appl. Phys.* **2018**, *52*, 013001. [CrossRef] [PubMed]
12. Akbar, A.A.; Ahammad, N.A.; Awan, A.U.; Hussein, A.K.; Gamaoun, F.; Tag-ElDin, E.M.; Ali, B. Insight into the Role of Nanoparticles Shape Factors and Diameter on the Dynamics of Rotating Water-Based Fluid. *Nanomaterials* **2022**, *12*, 2801. [CrossRef] [PubMed]

13. Yang, D.; Babucci, M.; Casey, W.H.; Gates, B.C. The Surface Chemistry of Metal Oxide Clusters: From Metal–Organic Frameworks to Minerals. *ACS Cent. Sci.* **2020**, *6*, 1523–1533. [CrossRef] [PubMed]

14. Chen, X.; Zhou, Y.; Roy, V.A.L.; Han, S. Evolutionary Metal Oxide Clusters for Novel Applications: Toward High-Density Data Storage in Nonvolatile Memories. *Adv. Mater.* **2017**, *30*, 1703950. [CrossRef]

15. Li, X.-N.; Wang, L.-N.; Mou, L.-H.; He, S.-G. Catalytic CO Oxidation by Gas-Phase Metal Oxide Clusters. *J. Phys. Chem. A* **2019**, *123*, 9257–9267. [CrossRef] [PubMed]

16. You, M.-H.; Li, M.-H.; Li, H.-H.; Chen, Y.; Lin, M.-J. The impact of metal cations on the photochemical properties of hybrid heterostructures with infinite alkaline-earth metal oxide clusters. *Dalton Trans.* **2019**, *48*, 17381–17387. [CrossRef]

17. Shafi, M.A.; Bouich, A.; Fradi, K.; Guaita, J.M.; Khan, L.; Mari, B. Effect of deposition cycles on the properties of ZnO thin films deposited by spin coating method for CZTS-based solar cells. *Optik* **2022**, *258*, 168854. [CrossRef]

18. Zemski, K.A.; Justes, D.R.; Castleman, A.W., Jr. ChemInform Abstract: Studies of Metal Oxide Clusters: Elucidating Reactive Sites Responsible for the Activity of Transition Metal Oxide Catalysts. *ChemInform* **2010**, *33*, 6136–6148. [CrossRef]

19. Yu, B.Y.; Kwak, S.-Y. Carbon quantum dots embedded with mesoporous hematite nanospheres as efficient visible light-active photocatalysts. *J. Mater. Chem.* **2012**, *22*, 8345–8353. [CrossRef]

20. Shinde, S.S.; Bansode, R.A.; Bhosale, C.H.; Rajpure, K.Y. Physical properties of hematite α-Fe_2O_3 thin films: Application to photoelectrochemical solar cells. *J. Semicond.* **2011**, *32*, 013001. [CrossRef]

21. Pellin, M.J.; Riha, S.C.; Tyo, E.C.; Kwon, G.; Libera, J.A.; Elam, J.W.; Seifert, S.; Lee, S.; Vajda, S. Water Oxidation by Size-Selected Co27 Clusters Supported on Fe_2O_3. *ChemSusChem* **2016**, *9*, 3005–3011. [CrossRef] [PubMed]

22. Altarawneh, M.; Ahmed, O.H.; Jiang, Z.T.; Dlugogorski, B.Z. Thermal recycling of brominated flame retardants with Fe_2O_3. *J. Phys. Chem. A* **2016**, *120*, 6039–6047. [CrossRef] [PubMed]

23. Oh, H.D.; Lee, S.W.; Kim, S.O.; Lee, J.K. Facile synthesis of carbon layer-entangled Fe_2O_3 clusters as anode materials for improved Li-ion batteries. *J. Power Sources* **2013**, *244*, 575–580. [CrossRef]

24. Alaei, S.; Jalili, S.; Erkoc, S. Study of Electronic and Magnetic Properties of (Fe_2O_3) n Clusters Using Density Functional Theory. *Quantum Matter* **2016**, *5*, 607–611. [CrossRef]

25. Shahpari, M.; Behjat, A.; Khajaminian, M.; Torabi, N. The influence of morphology of hematite (α-Fe_2O_3) counter electrodes on the efficiency of dye-sensitized solar cells. *Sol. Energy* **2015**, *119*, 45–53. [CrossRef]

26. Sivula, K.; Le Formal, F.; Grätzel, M. Solar Water Splitting: Progress Using Hematite (α-Fe_2O_3) Photoelectrodes. *ChemSusChem* **2011**, *4*, 432–449. [CrossRef] [PubMed]

27. Najaf, Z.; Nguyen, D.L.T.; Chae, S.Y.; Joo, O.S.; Shah, A.-u.-H.A.; Vo, D.-V.N.; Nguyen, V.-H.; Van Le, Q.; Rahman, G. Recent trends in development of hematite (α-Fe_2O_3) as an efficient photoanode for enhancement of photoelectrochemical hydrogen production by solar water splitting. *Int. J. Hydrogen Energy* **2021**, *46*, 23334–23357. [CrossRef]

28. Ren, D.; Gui, K.; Gu, S.; Wei, Y. Mechanism of improving the SCR NO removal activity of Fe_2O_3 catalyst by doping Mn. *J. Alloys Compd.* **2021**, *867*, 158787. [CrossRef]

29. Zhang, K.; Dong, T.; Xie, G.; Guan, L.; Guo, B.; Xiang, Q.; Dai, Y.; Tian, L.; Batool, A.; Jan, S.U.; et al. Sacrificial Interlayer for Promoting Charge Transport in Hematite Photoanode. *ACS Appl. Mater. Interfaces* **2017**, *9*, 42723–42733. [CrossRef]

30. Fradi, K.; Bouich, A.; Slimi, B.; Chtourou, R. Towards improving the optoelectronics properties of $MAPbI_{3(1-x)}B_{3x}$/ZnO heterojunction by bromine doping. *Optik* **2021**, *249*, 168283. [CrossRef]

31. Rakhshani, A.E. Preparation, characteristics and photovoltaic properties of cuprous oxide—A review. *Solid-State Electron.* **1986**, *29*, 7–17. [CrossRef]

32. Grossiord, N.; Kroon, J.M.; Andriessen, R.; Blom, P.W. Degradation mechanisms in organic photovoltaic devices. *Org. Electron.* **2012**, *13*, 432–456. [CrossRef]

33. Yu, W.; Zhang, J.; Peng, T. New insight into the enhanced photocatalytic activity of N-, C- and S-doped ZnO photocatalysts. *Appl. Catal. B Environ.* **2016**, *181*, 220–227. [CrossRef]

34. Pesci, F.M.; Wang, G.; Klug, D.R.; Li, Y.; Cowan, A.J. Efficient suppression of electron–hole recombination in ox-ygen-deficient hydrogen-treated TiO_2 nanowires for photoelectrochemical water splitting. *J. Phys. Chem. C* **2013**, *117*, 25837–25844. [CrossRef] [PubMed]

35. Abuilaiwi, F.A.; Awais, M.; Qazi, U.Y.; Afzal, A. Al^{3+} doping reduces the electron/hole recombination in photo-luminescent copper ferrite ($CuFe_{2-x}Al_xO_4$) nanocrystallites. *Boletín De La Soc. Española De Cerámica Y Vidr.* **2022**, *61*, 252–262. [CrossRef]

36. Sun, H.; Cao, Y.; Feng, L.; Chen, Y. Immobilizing photogenerated electrons from graphitic carbon nitride for an improved visible-light photocatalytic activity. *Sci. Rep.* **2016**, *6*, 22808. [CrossRef]

37. Te Velde, G.T.; Bickelhaupt, F.M.; Baerends, E.J.; Fonseca Guerra, C.; van Gisbergen, S.J.; Snijders, J.G.; Ziegler, T. Chemistry with ADF. *J. Comput. Chem.* **2001**, *22*, 931–967. [CrossRef]

38. Vicent-Luna, J.M.; Apergi, S.; Tao, S. Efficient Computation of Structural and Electronic Properties of Halide Per-ovskites Using Density Functional Tight Binding: $GFN_{1-x}TB$ Method. *J. Chem. Inf. Modeling* **2021**, *61*, 4415–4424. [CrossRef]

39. Eom, T.; Kim, W.J.; Lim, H.K.; Han, M.H.; Han, K.H.; Lee, E.-K.; Lebègue, S.; Hwang, Y.J.; Min, B.K.; Kim, H. Cluster Expansion Method for Simu-lating Realistic Size of Nanoparticle Catalysts with an Application in CO_2 Electroreduction. *J. Phys. Chem. C* **2018**, *122*, 9245–9254. [CrossRef]

40. Korzhavyi, P.; Abrikosov, I.A.; Johansson, B.; Ruban, A.V.; Skriver, H.L. First-principles calculations of the vacancy formation energy in transition and noble metals. *Phys. Rev. B* **1999**, *59*, 11693–11703. [CrossRef]

41. Ferrante, J.; Smith, J.; Rose, J. Universal Binding Energy Relations in Metallic Adhesion. *Tribol. Ser.* **1981**, *7*, 19–30. [CrossRef]

42. Majid, A.; Zahid, S.; Khan, S.U.D. Theoretical study of (TM) FeO$_3$ (TM = 3d transition metals) molecular clusters. *J. Nanoparticle Res.* **2020**, *22*, 1–20. [CrossRef]

43. Li, K.; Xue, D. Estimation of Electronegativity Values of Elements in Different Valence States. *J. Phys. Chem. A* **2006**, *110*, 11332–11337. [CrossRef] [PubMed]

44. Tiest, W.M.B.; Kappers, A.M. Physical Aspects of Softness Perception. In *Multisensory Softness*; Springer: Berlin, Germany, 2014; pp. 3–15. [CrossRef]

45. Vogiatzis, K.D.; Polynski, M.V.; Kirkland, J.K.; Townsend, J.; Hashemi, A.; Liu, C.; Pidko, E.A. Computational Approach to Molecular Catalysis by 3d Transition Metals: Challenges and Opportunities. *Chem. Rev.* **2018**, *119*, 2453–2523. [CrossRef]

46. Kumar, M.; Bhattacharyya, N.; Bandyopadhyay, D. Architecture, electronic structure and stability of TM@Ge(n)(TM = Ti, Zr and Hf; n = 1–20) clusters: A density functional modeling. *J. Mol. Modeling* **2012**, *18*, 405–418. [CrossRef]

47. Khan, I.; Jalilov, A.; Fujii, K.; Qurashi, A. Quasi-1D Aligned Nanostructures for Solar-Driven Water Splitting Ap-plications: Challenges, Promises, and Perspectives. *Solar RRL* **2021**, *5*, 2000741. [CrossRef]

48. Walter, M.G.; Warren, E.L.; McKone, J.R.; Boettcher, S.W.; Mi, Q.; Santori, E.A.; Lewis, N.S. Solar Water Splitting Cells. *Chem. Rev.* **2010**, *110*, 6446–6473. [CrossRef]

49. Merazga, A.; Al-Zahrani, J.; Al-Baradi, A.; Omer, B.; Badawi, A.; Al-Omairy, S. Optical band-gap of reduced gra-phene oxide/TiO$_2$ composite and performance of associated dye-sensitized solar cells. *Mater. Sci. Eng. B* **2020**, *259*, 114581. [CrossRef]

50. Hamadanian, M.; Jabbari, V.; Gravand, A.; Asad, M. Band gap engineering of TiO$_2$ nanostructure-based dye solar cells (DSCs) fabricated via electrophoresis. *Surf. Coatings Technol.* **2012**, *206*, 4531–4538. [CrossRef]

51. Arifin, Z.; Suyitno, S.; Hadi, S.; Sutanto, B. Improved performance of dye-sensitized solar cells with TiO2 nanopar-ticles/Zn-doped TiO$_2$ hollow fiber photoanodes. *Energies* **2018**, *11*, 2922. [CrossRef]